RSC Advances

PAPER

View Article Online
View Journal | View Issue

Check for updates

Cite this: *RSC Adv.*, 2025, **15**, 21898

Self-assembled micelle-based polypyrrole nanotube-incorporated copper oxide nanocomposite for the optical, structural and electrochemical detection of hydroquinone in water samples and HER application†

H. Ganesha,[ac] M. Vandana,[de] S. Sapna,[c] S. P. Vijaykumar,[c] Abdullah Ba Shbil,[c] D. S. Suresh,[c] Sharanappa Chapi,[d] Sutasinee Kityakarn,*[b] Sirikanjana Thongmee[a] and H. Devendrappa*[c]

Received 14th May 2025
Accepted 5th June 2025

DOI: 10.1039/d5ra03381k

rsc.li/rsc-advances

Recently, hydrogen has garnered significant attention as a renewable and environmentally friendly energy source. The majority of industrial hydrogen is produced by turning natural gas into hydrogen. In this case, the development of reliable, economical, and effective catalysts that can produce hydrogen from water with minimum electrical bias is one of the main objectives of large-scale electrolysis. One approach to achieving the practical application of electrocatalysts in the production of hydrogen is to use easily accessible electrocatalyst materials that can facilitate the oxidation of water. In this work, we report the synthesis of an electrocatalyst for the electrochemical detection of the hydroquinone (HQ) analyte molecule in water samples and H_2 production. A polypyrrole nanotube/copper oxide (PNT/CuO) nanocomposite was synthesized *via* the self-assembly of a soft template obtained through chemical polymerization and a one-pot hydrothermal method. The prepared material was characterized using various techniques to examine its crystal phase, functional groups, and surface morphology. An electrochemical study was conducted using a PNT glassy carbon electrode (GCE) and PNT/CuO GCE, and CV curves showed a large surface area with good oxidation behaviour towards the HQ analyte. The DPV analysis of the HQ analyte exhibited an LOD of 0.36 μM and a high sensitivity of 9.33 $\mu A\ \mu M^{-1}\ cm^{-2}$, with a linear range of 5–60 μM. The real sample analysis of the HQ analyte in a water sample showed recovery in the range of 97.45–102.61% with an RSD of 1%. These findings suggest that the PNT/CuO GCE sensor is a strong option for detecting the HQ analyte in real samples. Furthermore, the PNT/CuO GCE exhibited exceptional electrocatalytic activity for the HER (η = 330 mV and Tafel slope = 139 mV dec^{-1}), showing that the PNT/CuO GCE exhibits high activity as an electrocatalyst for H_2 generation.

1. Introduction

The advancement of sustainable energy sources is a crucial requirement for preserving the global ecosystem and addressing future energy requirements.[1] Hydrogen is often regarded as a prime energy source in sustainable energy systems owing to its significant energy density, favorable environmental impacts, and renewability.[2] In this case, water electrosplitting offers a viable method for the cost-effective and clean production of hydrogen, utilizing effective electrocatalysts for the hydrogen evolution reaction (HER).[3] The noble metal Pt is recognized as a catalyst with the highest efficiency for the HER because all reaction mechanisms are involved in the HER activity on this metal.[4] However, the high cost and restricted accessibility of Pt limit its widespread use in water electro-splitting devices. Therefore, transition metals such as Co, Cu, Ni, Zn and Fe doped with conducting materials have been recognized as potential replacements for Pt. To date, there has been a significant demand for the advancement of electrocatalysts that are affordable, abundant in nature, and exhibit outstanding efficiency.[5,6] Furthermore, potassium hydroxide is typically employed in water electrolysis to prevent the significant corrosion loss associated with acid/base electrolytes.[7] Consequently,

---

[a] *Department of Physics, Faculty of Science, Kasetsart University, Bangkok 10900, Thailand*

[b] *Department of Chemistry, Faculty of Science, Kasetsart University, Bangkok 10900, Thailand. E-mail: sutasinee.k@ku.th*

[c] *Department of Physics, Mangalore University, Mangalagangothri, 574199, India. E-mail: dehu2010@gmail.com*

[d] *Department of Physics, BMS College of Engineering, Bengaluru, 560019, India*

[e] *Center for Nano-Materials & Displays, BMS College of Engineering, Bengaluru, 560019, India*

† Electronic supplementary information (ESI) available. See DOI: https://doi.org/10.1039/d5ra03381k

the advancement of non-noble metal-based catalysts for the H_2 reaction in alkaline environments with considerable catalytic activity is crucial for the large-scale production of hydrogen. Besides, electrocatalyst active materials play a crucial role in various environmentally friendly and potential electrochemical applications, such as electrochemical detection, and mainly the HER.

In addition, hydroquinone (HQ) is an important chemical used in many fields such as industry, manufacturing, cosmetics, agriculture, medicine, food, photography, and the environment; it helps prevent damage from oxidation and acts as an antioxidant.[8] However, this chemical is a serious environmental pollutant because it is very toxic and do not break down easily. The large amounts of waste released by industry directly harm the environment, human health, animals, and plants, given that they can enter humans and animals through breathing, water, and food. The industries released a large amount of waste, which has a direct effect on environmental pollutants, human health, animals, and plants because it directly entered human and animal bodies through inhalation, water, and food. Thus, HQ is considered a highly carcinogenic chemical and serious hazard by the US Environmental Protection Agency, the European Union, and the International Agency for Research on Cancer.[9,10] Consequently, it is necessary to fabricate and develop highly efficient electrochemical materials for the detection of the HQ analyte and as electrocatalysts for HER.

Conducting polymers (CPs) and their derivatives have attracted tremendous attention due to their tunable electronic properties,[11] flexible surface morphology, easy doping and de-doping process, and lightweight nature, including polypyrrole (PPY),[12] poly(3,4-ethylenedioxythiophene) (PEDOT),[13] polythiophene (PTH),[14] and polyaniline (PANI),[15] which can be obtained *via* a versatile array of synthesis methods. These methods provide distinctive surface morphology, including the formation of nanofibers,[16] nanospheres,[17] and nanotubes.[18] In CPs, polypyrrole nanotubes (PNTs) are considered a promising option for electrochemical applications because of their nanotube shape, which has attracted significant attention from scientists and industry. They possess many useful features, such as small size, thin structure, strong chemical stability, excellent resistance, and unique fibrillary nanotubes, which help speed up electron transfer and support electro-oxidation activity.

The composition, dimension, and morphology of electrocatalysts significantly influence their electrochemical activity. Recently, several transition metal-derived electrocatalysts, such as transition metal hydroxides, sulfides, and oxides, including metal oxides such as RuO_2,[19] NiO,[20] MnO_2,[21] V_2O_5,[22] Co_3O_4,[23] ZnO, and CuO,[24,25] have been reported. Among them, CuO stands out as an exceptional electrode material due to its unique features, such as monoclinic phase structure, distinctive surface morphology, high stability, p-type semi-conducting nature, direct band gap in the range of 1.90 to 2.20 eV,[26] and moderately high absorption rate in the visible region with multiple oxidation states,[27] which exhibit potential biological properties and outstanding antimicrobial activity against environmental pathogens commonly found in water sources.[28,29] In the development of electrochemical sensors and electrocatalysts, a new avenue has been found in the utilization of composite materials; specifically, incorporating CuO in PNT composites has opened new possibilities in the development of electrochemical applications. The development of electrochemical sensors and electrocatalysts can be significantly boosted using these novel morphology materials, making them a more practical alternative to conventional electrocatalysts in a range of applications. It is clear from the literature survey that numerous research groups are diligently attempting to discover distinct conducting polymer-derived composite materials, including PPY/FCC-ZIF, which exhibited a unique surface morphology, where the addition of PPY enhanced the roughness of the electrode surface, which promoted the *in situ* growth of the catalyst. The abundant functional groups in the PPY can provide a large number of active sites, and the PPY molecular chain may contribute to the electrocatalyst activity.[30] M. J. Saadh *et al.* reported the integration of MOF@Fe_2O_3 as an efficient electrocatalyst for PPY. In their work, the composite material was observed to possess a high density of electrocatalytic active sites, which facilitated the adsorption of hydrogen species, and doping with Fe_2O_3 nanoparticles increased the electrical conductivity of the materials, enhancing their electrochemical properties.[31] A nanoporous faceted-based CuO electrocatalyst was used for solar to H_2 production, where an NF-based CuO film was prepared *via* a controlled polyesterification mechanism using a sol–gel spin coating technique, which was used for dual applications such as photo-electrochemical H_2 production and electrochemical nitrate reduction.[32] Also, a CuO/ZnO-doped rGO composite material was synthesized by a chemical reduction method. The synthesized electrocatalyst was examined in alkaline medium for its HER and OER activity. The CuO/ZnO-doped rGO showed a Tafel slope of 270 mV dec^{-1} for H_2 production.[33] A zinc oxide nanoflake-doped CuO nanocomposite was used as an electrocatalyst for water splitting, and due to the presence of mixed transition metals, it demonstrated a synergistic effect for H_2 production as a non-toxic material with a narrow band gap, which showed a Tafel value of around 400 mV dec^{-1}.[34] These research outcomes demonstrate the potential of CuO-based composite materials for use in future robust applications. These literature results were compared with the present work. PNTs and a PNT/CuO nanocomposite was synthesized *via* simple a cost-effective method, where CuO, which increased the surface area, exhibited multiple oxidation states and excellent electrical conductivity with a reduced band gap of 2.14 eV and a d-band electron in its valence shell. Also, PNTs contain π electrons in their backbone, and all these factors contributed to the high electrochemical activity of PNT/CuO GCE, which possessed a reduced Tafel slope of 139 mV dec^{-1} for HER. Additionally, the detection of HQ analyte demonstrated a sensitivity of 9.33 $\mu A\ \mu M^{-1}\ cm^{-2}$. Furthermore, we explored the dual application of H_2 production and detection as an electrochemical sensor, which may open new pathway for future research and practical application in the energy and environmental fields. Furthermore, doping CuO in conducting polymers (CPs) moderately changed their physicochemical properties; CuO possessed an extremely large surface area with high catalytic behavior. More interestingly, the physicochemical features of the PNT/CuO nanocomposite and its energy band gap had a significant impact on the electrochemical oxidation activity, and also enhanced the electrical conductivity, sensitivity, selectivity, electrocatalytic, and adsorption activity.

In the present work, we report the synthesis of PNTs and PNT/CuO nanocomposites through the self-assembly of micelle soft templates and a one-pot hydrothermal process. The fabricated electrode demonstrated a large area under the CV curve with a significant electrochemical response towards the HQ analyte. The DPV curve demonstrated its high sensitivity of 9.33 μA μM^{-1} cm^{-2} and low LOD of 0.36 μM with wide linearity. The PNT/CuO GCE material was very effective at detecting the HQ analyte, showing excellent recovery in real sample tests, and the electrocatalyst properties indicated Tafel plots of 183, 161, and 139 mV dec^{-1} for GCE, PNT GCE, and PNT/CuO GCE, respectively.

2. Experimental methods and materials

2.1 Materials used

$FeCl_3 \cdot 6H_2O$ (99.99%), C_2H_4NH monomer (98%), hydroquinone (99%), copper(II) oxide nanopowder (>50 nm), NaH_2PO_4, Na_2HPO_4, H_2SO_4, and methyl orange 4-(4-dimethylamino)phenylazo benzenesulfonic acid sodium salt (85%) were purchased from Sigma-Aldrich and Merck India, as analytical grade and used as received without further purification.

2.2 Synthesis of polypyrrole nanotubes

PNT nanotubes were synthesized through the self-degraded soft template polymerization method. Typically, 0.486 g of $FeCl_3$ and 0.098 g of methyl orange were dissolved in 60 mL of deionized water, and the solution was magnetically stirred for 60 min. Immediately, a flocculant precipitate formed, and then 200 μL pyrrole monomer was added to the above-mentioned solution. The color of the solution changed to black, and it was stirred for 24 h for polymerization. The PNT precipitate was obtained and washed with deionized water and ethanol multiple times, and then dried under vacuum at 50 °C overnight.

2.3 Synthesis of PNT/CuO nanocomposite

The PNT/CuO nanocomposite was synthesized *via* a one-step hydrothermal chemical process; 50 mg of PNTs and 0.25 g of CuO nanopowder were mixed in 60 mL of deionized water and vigorously stirred for one hour under sonication, and then the homogenously mixed solution was added to a Teflon-lined autoclave and maintained at 200 °C for 24 h. The black product was collected and washed with water and ethanol several times, and then dried at 50 °C in a vacuum overnight, as shown in Scheme 1.

3. Characterization techniques

X-ray photoelectron spectroscopy (XPS) was conducted on a Nexsa base model, and X-ray diffraction patterns were recorded using a Rigaku MiniFlex 600 instrument. Fourier transform infrared (FT-IR) spectra were measured in the range of 500 to 400 cm^{-1} with a spectral resolution of 4 cm^{-1} on a Bruker Alpha spectrometer. The Brunauer–Emmett–Teller (BET) analysis was performed using a Micromeritics 3Flex. Thermogravimetric measurements (TGA) were performed using a NETZSCH/STA instrument at a heating rate of 5 °C min^{-1} up to 800 °C. Field emission scanning electron microscope (FESEM) images were carried out using a Sigma Zeiss instrument.

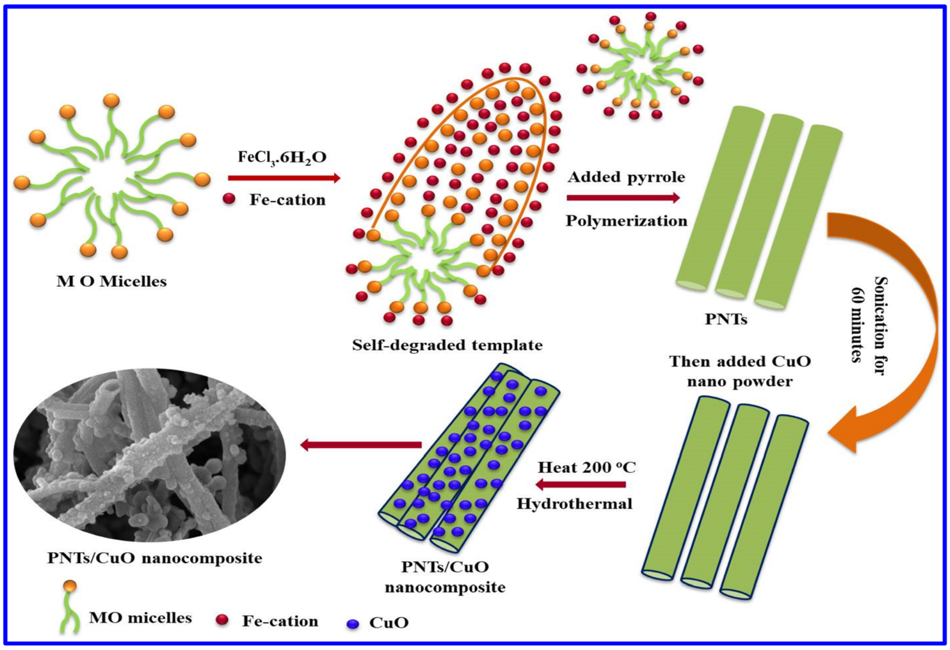

Scheme 1 Synthesis mechanism for PNTs and the PNT/CuO nanocomposite.

4. Electrochemical characterization techniques

The electrochemical sensing and H_2 production characterization, such as cyclic voltammetry (CV), differential pulse voltammetry (DPV), linear sweep voltammetry (LSV) and electrochemical impedance (EIS), were examined using a CHI660E electrochemical workstation. The LSV polarized curve were measured at a 10 mV s^{-1} scan rate in the presence of 0.5 M H_2SO_4. The determined potential (V *vs.* Ag/AgCl) values were converted to a reversible hydrogen electrode (RHE).

4.1 Fabrication of PNTs and PNT/CuO GCE

Sample preparation and working electrode fabrication: a glassy carbon electrode (GCE) was used as the working electrode with a 3 mm diameter. The GCE was pre-treated using an alumina slurry at different thickness of 1.0 μm, 0.3 μm and 0.05 μm on a polishing pad. Then, GCE was rinsed with H_2O and H_2SO_4 (1 : 1, v/v). Subsequently, the synthesized material/PVDF/activated charcoal (90 : 5 : 5 wt%), which was homogenously dispersed with Nafion solution, and the mixed homogenous slurry were drop-casted on the GCE surface and dried for 12 h at 60 °C, and then the dried electrode was used for electrochemical applications.

5. Results and discussion

5.1 Material, structural, and optical characterization and techniques

Fig. 1(a and b) show the FESEM images of pure PNTs, showing a well-defined, uniformly arranged nanotube with a diameter of about 166 nm. The formation of the nanotube morphology significantly depends on various factors such as the concentration of the solution, soft template M.O., and magnetic stirring time. Fig. 1(c and d) show the FESEM images of PNT/CuO nanocomposites, showing CuO deposited on the surface of PNTs, and the average diameter of the nanotube is 266.4 nm.

Interestingly, even with the incorporation of CuO in the PNTs, the nanotube structure maintained a good tubular morphology. The metal oxide and polymer composite effectively prevented the agglomeration of the nanostructure, while the combination of organic and inorganic materials in the nanotube morphology contributed to achieving high electrocatalytic oxidation activity.

Fig. 1(e and f) present the EDS analysis of the PNT and PNT/CuO nanocomposite material, respectively. The EDS analysis of the PNTs and CuO incorporated in the PNTs confirmed the presence of carbon (C) and nitrogen (N), and copper (Cu) and oxygen (O), which revealed the atomic percentages of 45.51% and 54.49%, and 47.62%, 29.07%, 12.74% and 10.57%, in addition to weight proportions of 49.34% and 50.66% and 50.32%, 27.39%, 13.57% and 8.72% for the PNTs and PNT/CuO materials, respectively. As shown in Fig. S1(a, b) and (c–f),† the observed elemental mapping images exhibit a homogeneous distribution of C, N, Cu, and O elements for the PNT and PNT/CuO materials.

In good agreement with the reported FESEM pictures, the HR-TEM images of the PNT/CuO nanocomposite show that the CuO nanoparticle structure has uniform distribution over the core surface of the PNTs. Also, the PNT/CuO nanocomposite exhibited an observable contrast within the dark and bright zones; a PNT is represented by the bright region, while a CuO nanoparticle is represented by the dark zone, as shown in Fig. 1(g and h), respectively. This clearly indicates the homogeneous distribution of CuO nanoparticles in the composite material, which enhances the atomic defects in the composite and beneficial for generating active sites during the electrochemical process, and also improve the oxidation and H_2 production activity.

Fig. 2(a) shows the XRD pattern of PNTs and PNT/CuO nanocomposite, where PNTs demonstrate a broad peak at the 2θ value of 26.6°, which confirms the polymerization of the pyrrole chain in the PNTs. The XRD pattern of PNT/CuO possessed distinctive peaks at 32.79°, 35.71°, 38.90°, 49.13°, 53.97°, 58.59°, 61.89°, 66.51°, 68.42°, 72.82°, and 75.46°, which are indexed to the (110), (−111), (111), (−202), (020), (−113), (−311), (220), (311) and (−222) crystal planes, respectively. These results reveal that CuO is a monoclinic structure and are in good agreement with previously published values.[35] Also, the low-intensity broad peak located at 26.6° revealed that the PNTs were uniformly incorporated in the CuO nanocomposite, showing the strong interaction of CuO and PNTs in the nanocomposite.

Fig. 2(b) shows the FTIR spectra of PNTs and PNT/CuO nanocomposites, where PNTs exhibit a prominent characteristics peak at 1535 cm^{-1}, which is related to the C=C stretching vibrational mode of the pyrrole ring, and a peak at 1337 cm^{-1} corresponding to the C–H stretching in the PNT ring. The peak located at 1184 cm^{-1} is attributed to the C–N stretching vibrational of the pyrrole ring,[36,37] the observed deformed peak at 1044 cm^{-1} is related to the C–H in-plane bending, and the peak located at 909 cm^{-1} corresponding to the polymerization of pyrrole. The sharp intense and wagging peaks at 516 cm^{-1} and 647 cm^{-1} represent the presence of Cu–O in the composite,[38,39] which are not present in the in spectrum of PNTs.

Fig. 3(a) shows the absorption spectrum of PNTs, which exhibits two peaks at 265 nm and 446 nm associated with the π to π^* transition.[40,41] When nano-CuO was embedded on the surface of PNTs, these peaks shifted for the nanocomposite towards a higher wavelength at 269 nm and redshifted to 469 nm, respectively. These results indicate that the electron band gap decreased in the presence of CuO, which reveals the proper chemical interaction in the PNT/CuO nanocomposite. Fig. 3(b) illustrates the optical band gap and Tauc plot of the PNTs and PNT/CuO nanocomposite. The direct band gap can be determined by graphically plotting $(\alpha h\nu)^2$ *vs.* $h\nu$ using the mathematical formula

$$\alpha = A(h\nu - E_g)^n/h\nu$$

where n represents the direct band gap value, which is $\frac{1}{2}$, A represents a constant, E_g indicates the material energy gap, and α refers to the absorption coefficient rate.[42]

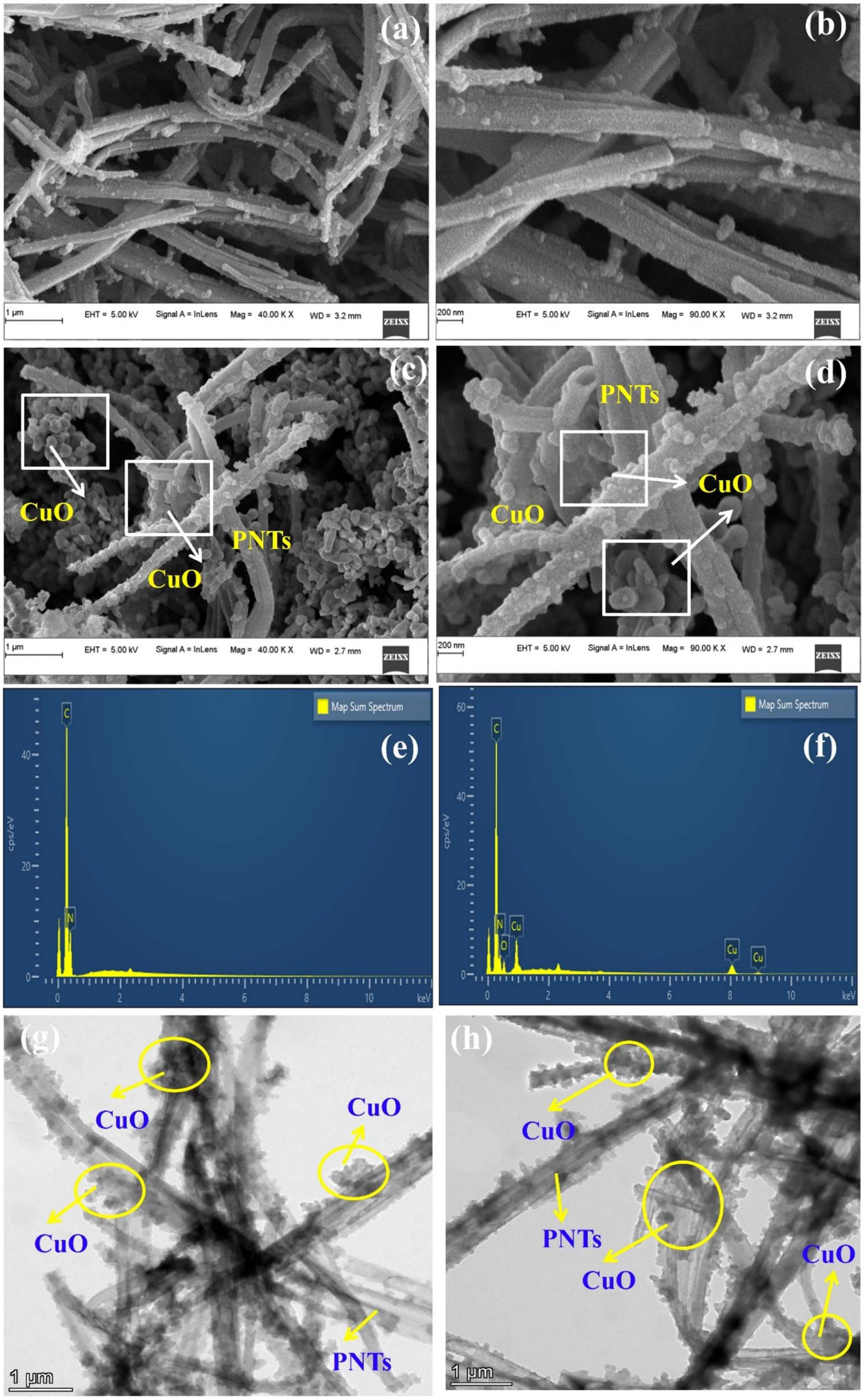

Fig. 1 FESEM images of (a and b) PNTs and (c and d) PNT/CuO at different resolutions and (e and f) EDS and (g and h) HR-TEM images of the PNT/CuO nanocomposite.

The band gaps were calculated to be 2.22 and 2.14 eV for PNTs and PNT/CuO nanocomposite. The E_g band gap of the PNT/CuO nanocomposite is lower than that of PNTs because it can effectively establish transition of charge carriers and the generation of defects in localized states in the optical band gap due to the incorporation of CuO metal ions in the polymer matrix (Table 1).

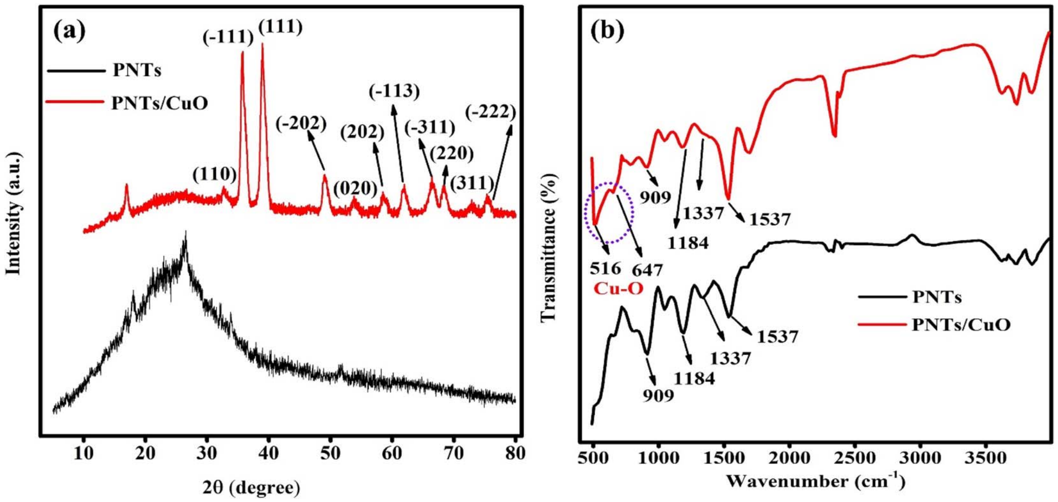

Fig. 2 XRD patterns (a) and FTIR (b) spectra of PNTs and the PNT/CuO nanocomposite.

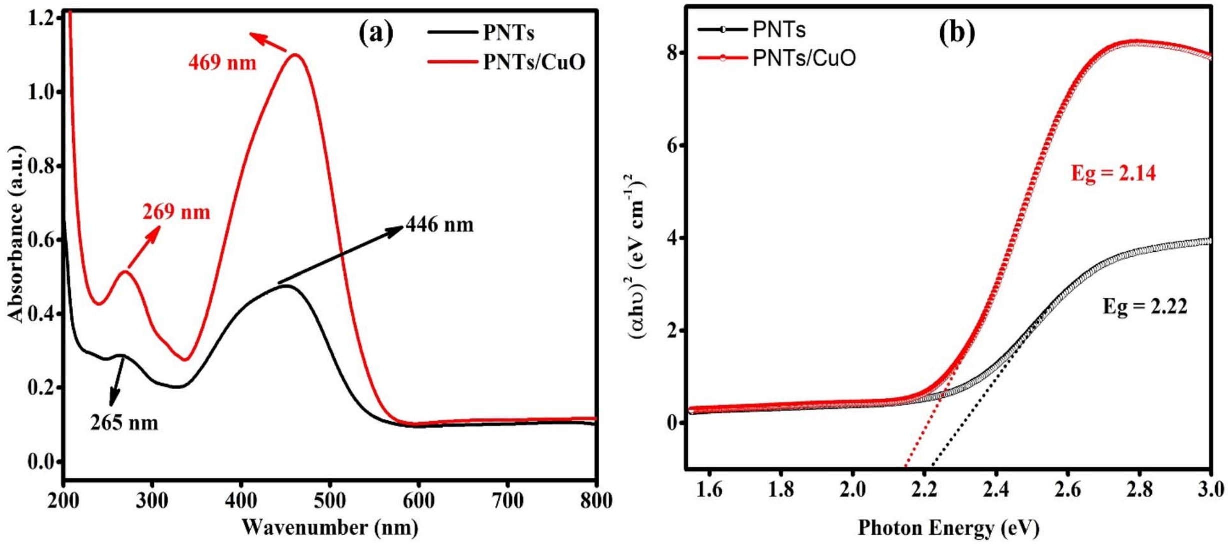

Fig. 3 UV-visible absorption spectra (a) and optical band gap photon energy curve (b) of PNTs and the PNT/CuO nanocomposite.

Table 1 The determined direct band gap values for PNTs and the PNT/CuO nanocomposite

S. no.	Name of the material	E_g direct band gap (eV)
1	PNTs	2.22
2	PNT/CuO nanocomposite	2.14

Fig. 4(a) shows the XPS spectrum of Cu 2p, which was deconvoluted into Cu $2p_{3/2}$ and Cu $2p_{1/2}$ with three distinct satellite peaks located at 941.16 eV, 944.02 eV, and 962.66 eV, corresponding to the characteristics of Cu–O. The Cu $2p_{3/2}$ spectra exhibit two peaks at 933.03 eV and 934.52 eV, which are assigned to the tetrahedral and octahedral Cu and Cu^{2+} ions, respectively, and the Cu $2p_{1/2}$ peak is located at the binding energy of 952.85 eV.[43,44] The binding energy difference between Cu $2p_{3/2}$ and Cu $2p_{1/2}$ is 19.82 eV, which reveals the successful formation of CuO in the PNT/CuO nanocomposites. Fig. 4(b) shows the O 1s spectrum, which was deconvoluted into two peaks, with the major peak located at 529.96 eV ascribed to the oxygen atoms of Cu–O, and the peak at 531.43 eV related to the –OH– hydroxyl group from the surface of Cu–O.[45,46] Fig. 4(c) shows the C 1s spectrum, demonstrating three peaks, with a prominent peak at 284.74 eV corresponding to C–C, and the peaks at 285.63 eV and 287.12 eV belonging to the alkyl chains and cyclic amidic C=O– in polypyrrole, respectively.[47–49] As shown in Fig. 4(d), the observed N 1s core level spectrum shows two peaks at 399.57 eV, and 400.35 eV, which are associated with the neutral amine and nitrogen group (–NH–) and positively charged nitrogen chain in the pyrrole ring (–N^+–), respectively,

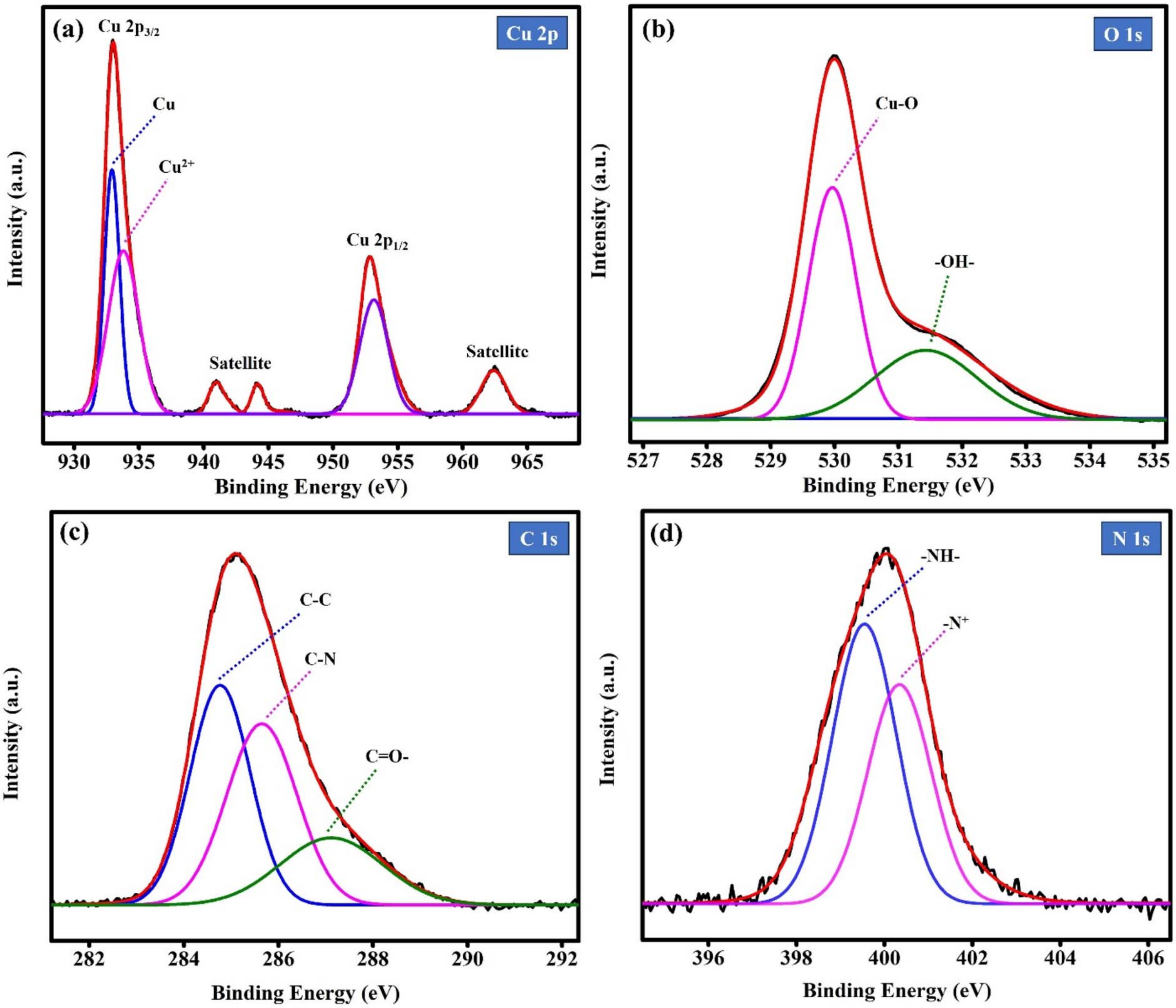

Fig. 4 XPS spectra of the PNT/CuO nanocomposite (a) Cu, (b) O 1s, (c) C 1s and (d) N 1s elements.

suggesting the existence of PNTs in the PNT/CuO nanocomposite material.[50]

The FESEM images distinctly illustrate that the composites of PNTs and CuO exhibit a nanotube structure. The adsorption characteristics and surface properties of the nanocomposite materials were investigated using the BET method in a nitrogen environment and recording their adsorption–desorption isotherms at ambient temperature. Fig. 5(a) illustrates the nitrogen gas adsorption–desorption isotherms of PNTs and PNT/CuO. According to the multi-point BET analysis, the specific surface area of PNTs and PNT/CuO composite was found to be 28.62 and 76.25 $m^2\ g^{-1}$, respectively. Upon the integration of PNTs with the metal oxide, the composite exhibited an enhanced specific surface area, and the plot exhibits a type IV isotherm,[51] which indicates the presence of a mesoporous structure. The composite exhibited a specific surface area and porosity that revealed an increased number of redox active sites for ion–electron diffusion, ultimately leading to an improved electrochemical performance.[52]

The pore size and volume distribution of the synthesized material were examined using the BJH technique, as displayed in Fig. 5(b and c). The observed pore diameters for PNTs and PNT/CuO nanocomposite are approximately 18.256 nm and 12.751 nm, respectively. Therefore, these results confirmed that the synthesized materials are mesoporous structures, which increased their surface area, resulting in a greater number of active sites. The PNT/CuO nanocomposite has a wide surface area. This makes it an ideal candidate for electrochemical applications.

The thermal stability of PNTs and PNT/CuO nanocomposite is displayed in Fig. 5(d). The thermal stability of the materials was examined at temperatures in the range of 30 °C to 700 °C at a heating rate of 10 °C min^{-1} in a nitrogen environment with a flow rate of 50 mL per minute to record the TGA curves. The thermograms of PNTs and the PNT/CuO nanocomposite showed two stages of weight loss. Initially, there was only a slight weight loss of approximately 6.5% at 430 °C and 3% at 490 °C, respectively. The primary cause of the weight loss is residual solvent moisture, and the water content from the polymer matrix is responsible for the initial stage weight loss.[53] In the case of the second stage, the weight loss began at 450 °C to 605 °C and 505 °C to 624 °C for PNTs and PNT/CuO

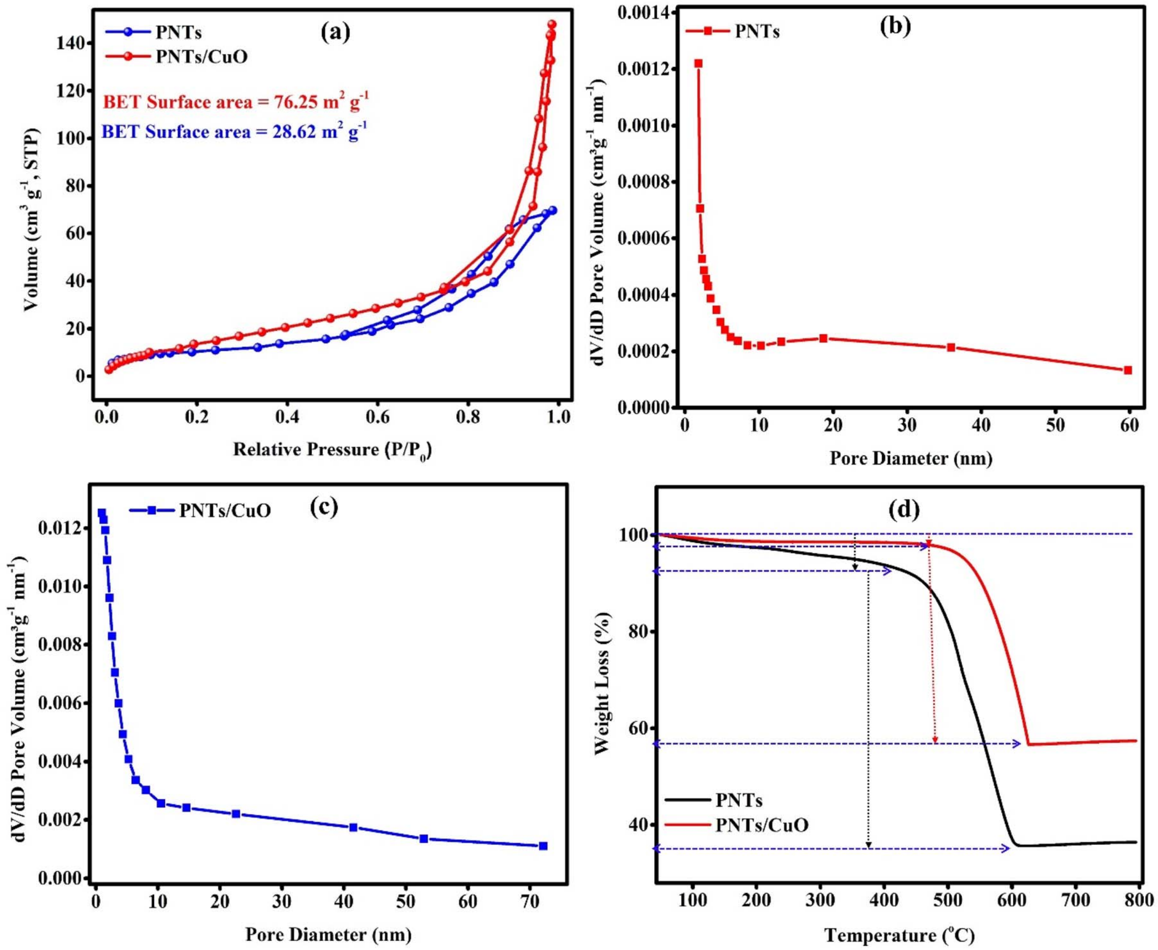

Fig. 5 (a) BET isotherms, (b and c) BJT pore size and diameter and (d) TGA analysis of PNTs and the PNT/CuO nanocomposite.

nanocomposite, respectively. The PNT/CuO nanocomposite exhibited superior thermal stability across the whole temperature range, whereas in the case of pure PNTs, the breakdown of their polymer chains caused a considerable weight loss in the second stage.[54] The PNT/CuO nanocomposite demonstrated excellent thermal resilience with thermal stability up to 624 °C.

6. Electrochemical sensing parameters

6.1 CV curve analysis in absence and presence of HQ

Fig. 6(a) demonstrates the CV curves of the bare GCE, PNT GCE, and PNT/CuO GCE in the absence of HQ analyte, where the bare GCE and PNT GCE showed no peak at the oxidation and reduction current, possessing low electrochemical oxidation behaviour. In contrast, the CV curve of PNT/CuO GCE displays redox behaviour with a large surface area and the peak current response was found to be 21.36 μA, which is higher than that of the bare GCE and PNT GCE of 8.23 μA and 14.81 μA, respectively. These results suggest that the PNT/CuO GCE electrode material may promote the detection ability of analyte species.

Fig. 6(b) shows the electrochemical behaviour of the bare GCE, PNT GCE, and PNT/CuO GCE CV, where the curves were examined in the presence of a 100 μM HQ analyte. Bare GCE showed low oxidation activity in the presence of the HQ analyte, while PNT GCE showed a predominant oxidation peak. This indicates that the PNT GCE easily showed electrochemical oxidation activity for the HQ analyte due to its positively charged nitrogen group and amine functional group, facilitating the contact between the surface of the electrode material and electrolyte. Consequently, it instantly adsorbs the analyte species of HQ. Also, PNT/CuO GCE showed good oxidation activity towards the detection of HQ analyte because of its oxygen and metallic functionalities, enabling it to quickly oxidize the target HQ analyte. Its electrochemical responses are indicated by the changes in the shape of its CV curve, which exhibits the wide surface area under the CV curve, and its peak current was found to be 50.79 μA higher than that of PNTs of 34.56 μA. This result indicates that the conducting polymer combined with metallic oxide creates an accessible surface area with high conductivity, which improves the electron transfer and sensing capability in the material.

6.2 Effect of scan rate

Fig. 7(a) shows the CV curves of PNT/CuO GCE measured at different scan rates in the presence of 100 μM HQ analyte. With

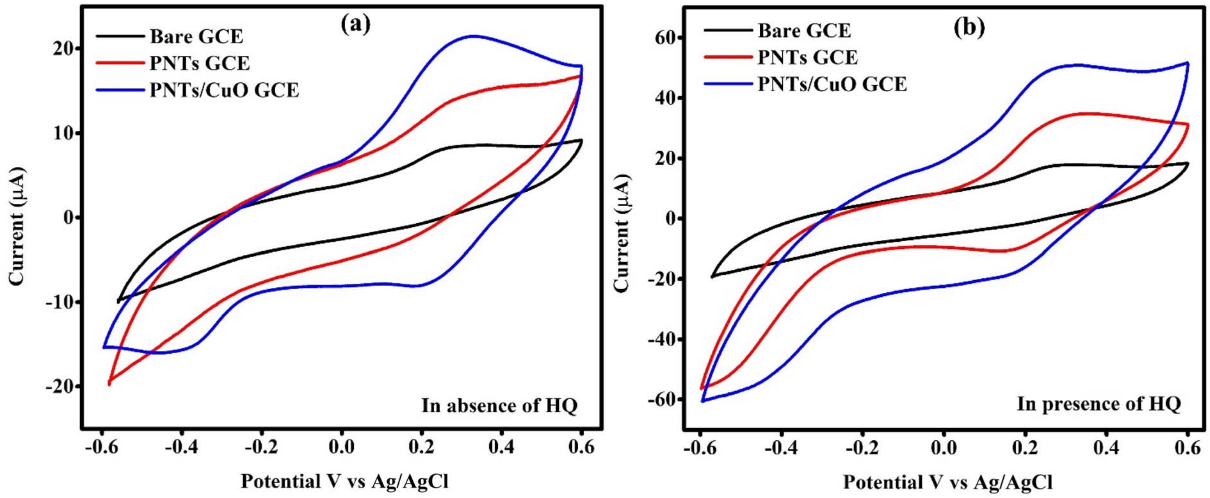

Fig. 6 CV curves of (a) the bare GCE, PNT GCE, and PNT/CuO GCE in the absence of the HQ analyte and (b) bare GCE, PNT GCE, and PNT/CuO GCE in the presence of 100 μM HQ containing 0.1 M PBS electrolyte (pH 7.0).

an increase in the scan rate from 10 mV s^{-1} to 50 mV s^{-1}, the intensity of the oxidation peak current linearly shifted towards a higher current density, but the CV curve maintained the same shape, which signifies that the peak current is directly proportional to the scan rate. Fig. 7(b) shows the calibration plot of peak current *versus* scan rate of the PNT/CuO GCE, which exhibits a linear relationship between peak current and scan rate as follows:

$$I_P = 0.7765C + 15.9385; (R^2 = 0.990)$$

This value suggests that the PNT/CuO GCE electrochemical detection follows a diffusion-controlled process.[55]

The PNT/CuO GCE showed a superior synergistic effect, which is mainly attributed to the interaction between the PNTs and CuO, and the nanotube morphology can provide a huge surface area, high conductivity, and abundant active sites, and create a passageway for the transfer of electrons in the electrolyte, which are beneficial for adsorbing the sensing analyte, and also increase the electrochemical oxidation behaviour.[56]

6.3 DPV and EIS analysis

Fig. 8(a) displays the DPV analysis of PNT/CuO GCE, where the electrochemical detection activity was examined by adding different concentrations of HQ analyte from 5 to 60 μM to the 0.1 M PBS supporting electrolyte (pH 7.0). With an increase in the concentration of HQ analyte, the surface of the PNT/CuO GCE electrode rapidly adsorbed the HQ analyte, gradually enhancing the intensity of the oxidation current rate, which indicates that the PNT/CuO GCE electrochemical oxidation reaction is fast and it quickly detected the target analyte molecule. This is attributed to the nanotube morphology, which can easily establish a passageway for electron transfer in the electrolyte and beneficial for increasing the electrochemical oxidation process.

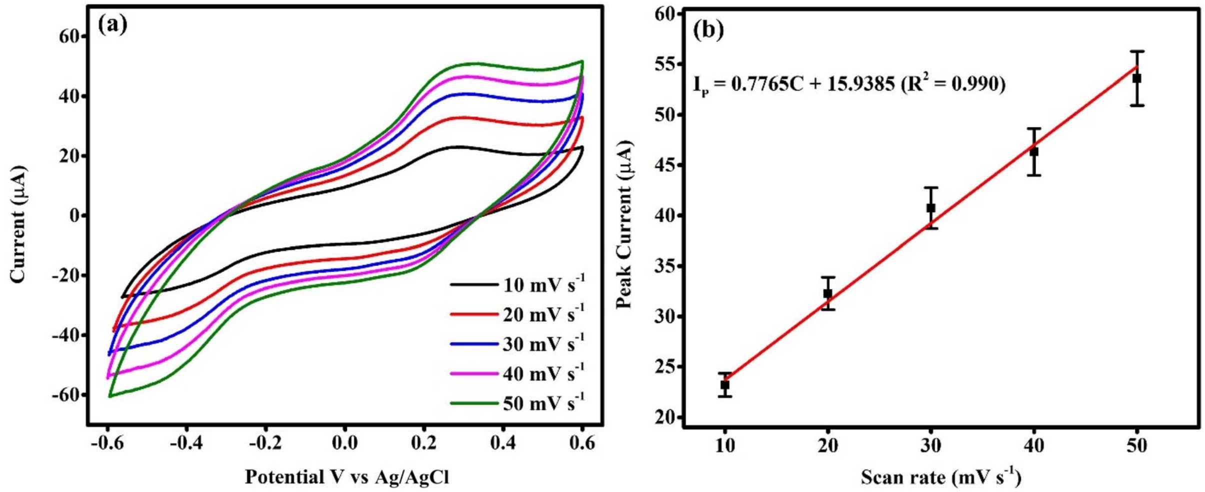

Fig. 7 (a) PNT/CuO GCE CV curves recorded at different scan rates (10–50 mV s^{-1}) and (b) calibration curve of the peak current against scan rate.

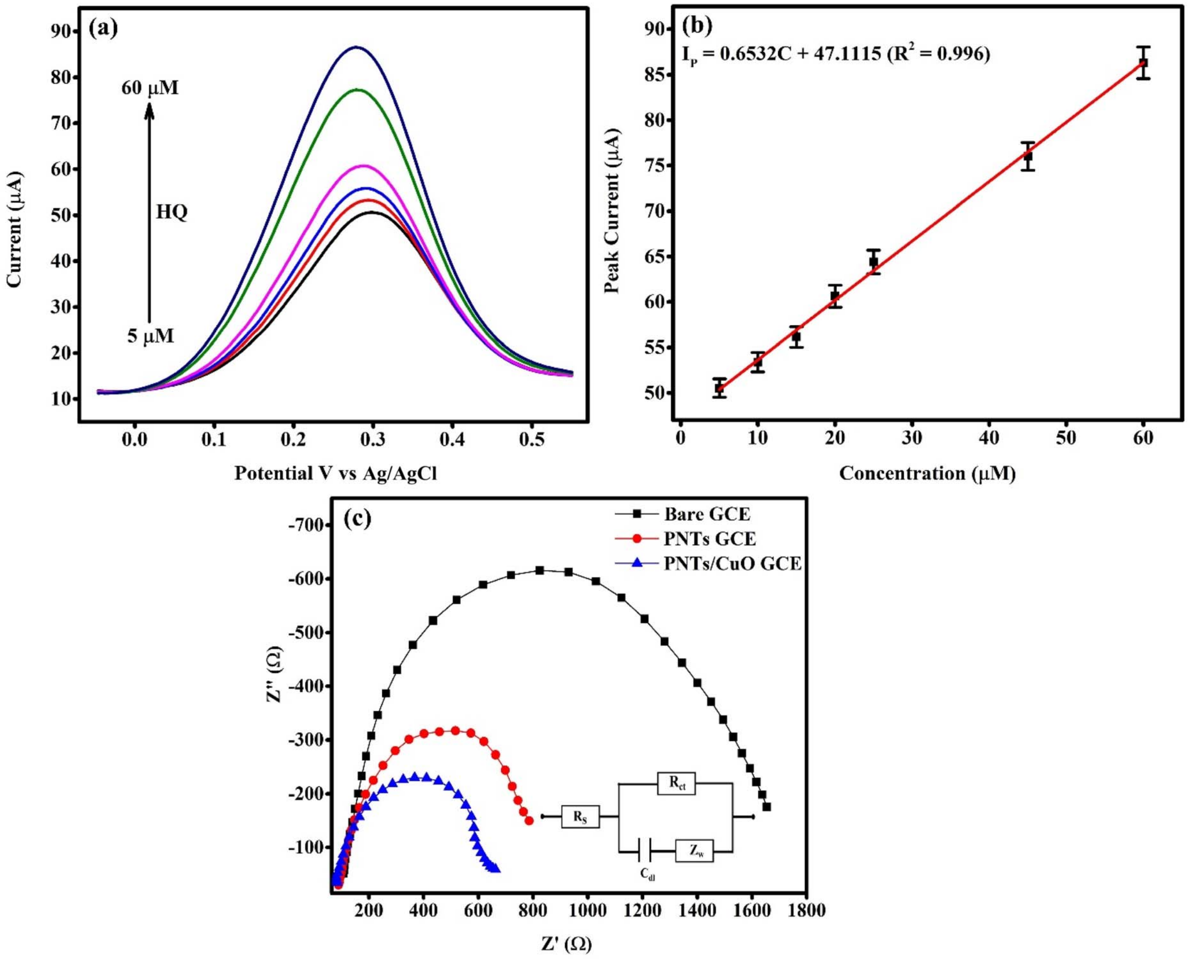

Fig. 8 DPV analysis of the PNT/CuO GCE in the HQ analyte (a), linear calibration plot of peak current as a function of the concentration of HQ (b) and (c) EIS spectra of the bare GCE, PNT GCE and PNT/CuO GCE (inset figure is the equivalent circuit).

Fig. 8(b) demonstrates the HQ calibration plot of PNT/CuO GCE, where various concentrations of HQ analyte were successively added to 0.1 M PBS electrolyte, and the intensity of the oxidation peak current gradually increased. The calibration plot of PNT/CuO GCE peak current (I_P) *vs.* concentration of HQ was used to obtain the linear equation and correlation co-efficient as follows:

$$I_P\ (\mu A) = 0.6532[HQ] + 47.1115;\ (R^2 = 0.996)$$

The observed values reveal that the electrochemical detection reaction for the HQ target analyte is controlled by a diffusion process, and the determined limit of detection (LOD) for HQ by PNT/CuO GCE was 0.36 μM and its sensitivity was found to be 9.33 μA μM^{-1} cm^{-2}, with a wide linear range of 5 μM to 60 μM. These results indicate that the PNT/CuO nanocomposite possesses a wide surface area and abundant active sites, which could induce rapid electron transfer in the electrolyte and enhance the oxidation activity. Also, the PNT/CuO GCE oxidation of HQ analyte involved a two-electron and two-proton transfer mechanism.

The observed LOD, linearity, and sensitivity for HQ analyte are higher values compared to previously reported electrode materials,[57–61] as mentioned in Table 2.

The electrical charge resistance characteristics and the interface electrode surface of PNTs and PNT/CuO GCE in the presence of 100 μM HQ analyte were investigated using the EIS technique. The Nyquist plot shows the ideal semicircle arc and the diameter of the semicircle arc associated with the charge transfer resistance (R_{ct}), as shown in Fig. 8(c). PNT/CuO GCE achieved the low R_{ct} of 654 Ω, while that of the PNT GCE and bare GCE was found to be 783 and 1654 Ω, respectively. This is mainly due to the presence of oxygen vacancies and nitrogen functionality, which facilitate the wide surface area and high conductivity, creating a passageway for electron transfer in the electrolyte and easily oxidizing the target analyte, thus establishing the high oxidation activity.

6.4 Selectivity study

Furthermore, the selectivity of the PNT/CuO GCE for the HQ analyte was studied in the presence of a 10-fold higher concentration of possible interferences and salts such as

Table 2 Comparison of the electrochemical detection of the HQ analyte by different electrode materials

Electrode materials	Technique	Determined LOD (μM)	Linearity (μM)	Sensitivity (μA μM^{-1} cm^{-2})	Ref.
rGO/L-cys	DPV	1.5	2–160	—	57
Ce/MOF/CNTs/GCE	DPV	5.3	10–100	—	58
Poly/MCPE	CV	2.1	10–45	—	59
rGO/LRT/GCE	DPV	0.75	1–100	—	60
TrGO	DPV	0.75	1–500	—	61
PNT/CuO GCE	**DPV**	**0.36**	**5–60**	**9.33**	**This work**

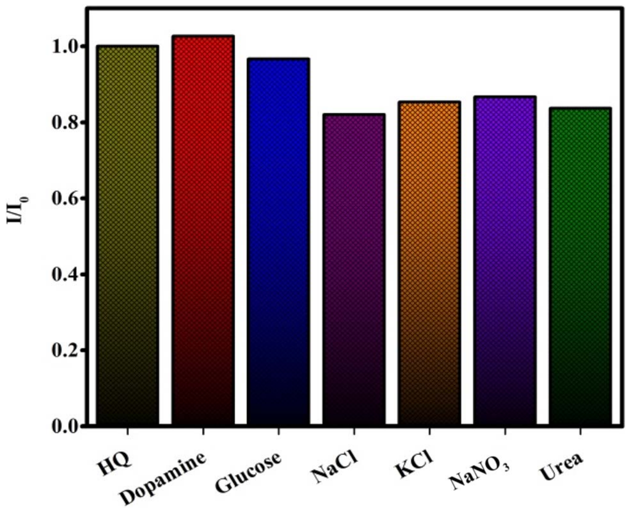

Fig. 9 Selectivity study of the PNT/CuO GCE for HQ analyte examined in the presence of different interferences and salts.

Table 3 Real sample analysis of HQ detection in water samples

Sample	Spiked (μM)	Found (μM)	Recovery (%)	RSD (%)
Tap water	50	50.94	101.88	0.16
	60	59.57	99.29	0.38
River water	50	51.30	102.61	0.57
	60	58.47	97.45	1.00

dopamine, glucose, NaCl, KCl, $NaNO_3$, and urea, and the bar graph is depicted in Fig. 9 and S2.† The results indicated that the interference substances had a negligible influence on the HQ analyte and the RSD is below 2%, which is an acceptable value, indicating that the PNT/CuO GCE has good practical application as a sensor.

6.5 Real sample analysis

Tap water and local river water were used to examine the practical applicability of the PNT/CuO GCE, as shown in Fig. S3(a–d).† The detection of HQ in tap water and river water was measured using the standard addition method. The obtained experimental results were satisfactory with a recovery in the range of 97.45% to 102.61% with a relative standard deviation (RSD) of 1%, as listed in Table 3. These results prove that the fabricated sensor electrode has superior potential towards the determination of real samples.

6.6 Study of electrocatalytic HER activity

The LSV polarization method was used to investigate the electrocatalytic activity of bare GCE, PNT GCE, and PNT/CuO GCE materials for HER application in 0.5 M H_2SO_4 at a potential scan rate of 5 mV s^{-1}. The LSV polarization activity of bare GCE, PNT GCE and PNT/CuO GCE is shown in Fig. 10(a). The observed potential (V *vs.* Ag/AgCl) values were converted to RHE using the following mathematical equation:

$$E_{\mathrm{RHE}} = E_{(\mathrm{Ag/AgCl})} + 0.059(\mathrm{pH}) + 0.197$$

where E_{RHE} represents the reversible hydrogen electrode, $E_{(\mathrm{Ag/AgCl})}$ signifies the reference electrode and pH denotes the acidic/alkali value of the electrolyte solution. The bare GCE and PNT GCE exhibit an overpotential of 390 mV and 352 mV at a current density of 10 mA cm^{-2}, respectively. Notably, the PNT/CuO GCE showed a relatively low overpotential, which is a 330 mV than the other electrocatalyst material due to the deposition of metal oxide on the surface of PNTs, which resulted in an excellent overpotential with superior current density. Fig. 10(b) illustrates the bar plot of the overpotential *versus* different electrocatalyst materials. This result indicates that the effective incorporation of PNTs and CuO improved the electrocatalytic abilities of the PNT/CuO GCE. This enhancement is attributed to the significant electroactive surface area, abundance of electro-catalytic active sites, improved conductivity, synergistic effects, and the fibrous morphology of the material. Further, the HER polarization curve was examined through the analysis of the Tafel slope, as shown in Fig. 10(c). The Tafel slope provides a crucial parameter to determine the rate-limiting process in the HER activity, which corresponds to the current density at the specified potential. The lower Tafel slope and greater current density of the electrocatalyst material indicate enhanced HER activity. The observed Tafel slope values for bare GCE, PNT GCE and PNT/CuO GCE are 183, 161 and 139 mV dec^{-1}, respectively. Among the electrodes, considering that PNT/CuO GCE has the lowest Tafel slope, it is a highly active H_2 electrocatalyst. This finding confirms that the PNT/CuO GCE composition, activated by H_2SO_4, is an extremely efficient electrocatalyst to increase the rate of HER. Fig. 10(d) displays a bar graph of the Tafel slope of different

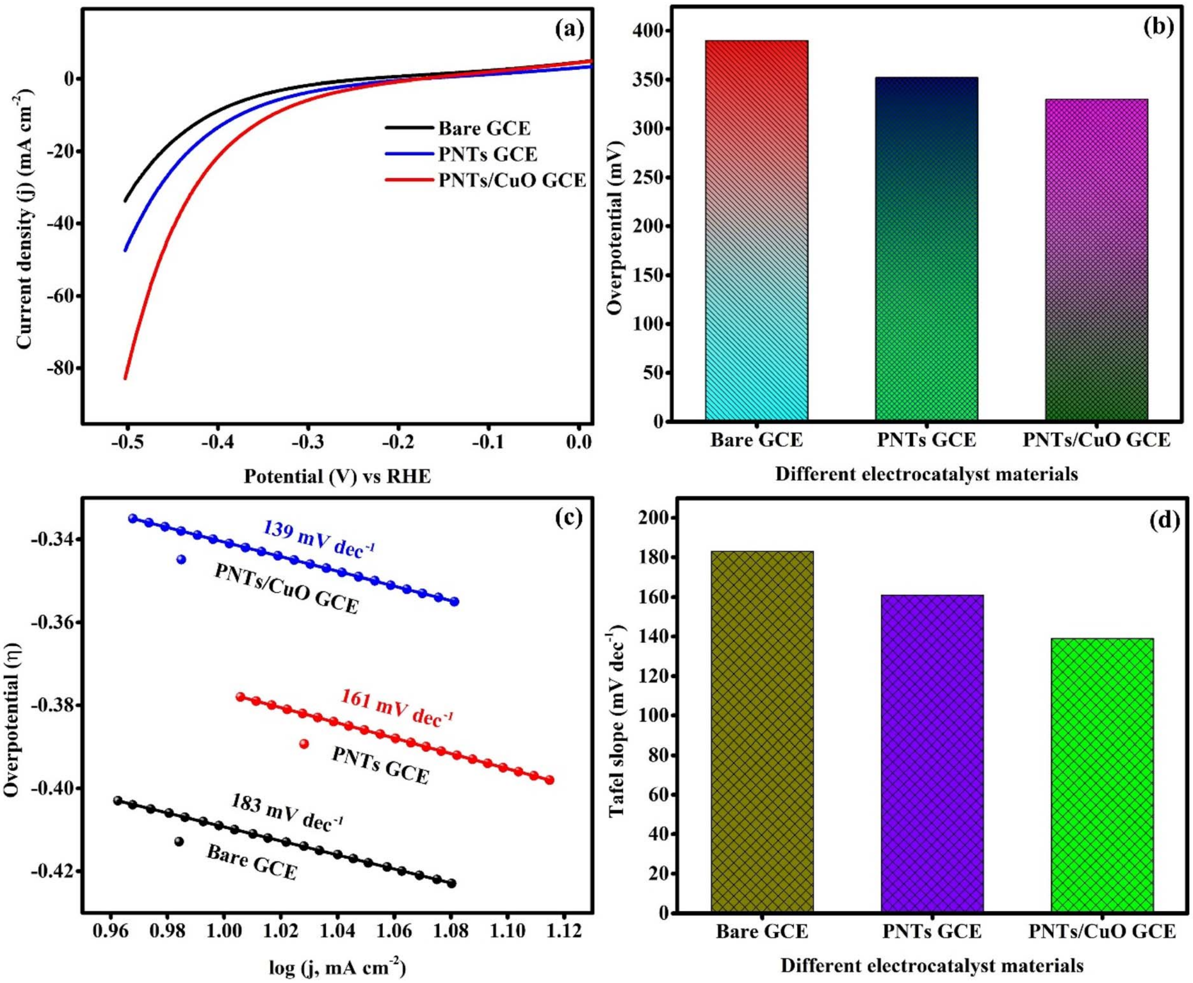

Fig. 10 (a) LSV polarization curve of the bare GCE, PNTs GCE, and PNT/CuO GCE electrocatalyst at a scan rate of 5 mV s^{-1}. (b) Overpotential bar graph of the different electrocatalyst materials. (c) Tafel slopes and (d) bar graph of the Tafel slope for the corresponding electrocatalyst materials.

Table 4 Comparison of the performance of previously reported electrocatalyst materials

Electrocatalyst material	η (mV) at 10 mA cm^{-2}	Tafel slope (mV dec^{-1})	Electrolyte	Ref.
CuO/Cu$_2$O@Mn50	355	90.60	1.0 M KOH	62
CPE-1	565	139	0.5 M H$_2$SO$_4$	63
CPCE-1	516	160	0.5 M H$_2$SO$_4$	64
PANI@MOF	—	180	1.0 M KOH	65
Cu/MOF	660	224.6	0.5 M H$_2$SO$_4$	66
PNT/CuO GCE	330	139	0.5 M H$_2$SO$_4$	This work

electrocatalyst materials. The PNT/CuO GCE catalyst exhibited the greatest electrocatalyst activity, with notable enhancements in the catalytic efficiency noted upon the introduction of the metal oxide composition in the conducting polymer. Interestingly, PNT/CuO GCE exhibited a superior performance as an electrocatalyst compared to PNT GCE. Furthermore, the obtained values are higher than previously reported electrocatalyst materials such as CuO/Cu$_2$O@Mn50 (η = 355 mV and Tafel slope = 90.60),[62] CPE-1 (η = 565 mV and Tafel slope = 139),[63] CPCE-1 (η = 516 mV and Tafel slope = 160),[64] PANI@MOF (Tafel slope = 180),[65] and Cu/MOF (η = 660 mV and Tafel slope = 224.6).[66] A comparison of the performance of different electrocatalyst materials is shown in Table 4.

7. Conclusion

In this summary, we designed a simple method for the synthesis of PNTs and PNT/CuO nanocomposite. The prepared core/shell nanotube composition exhibited several noteworthy benefits, such as a core/shell nanotube structure, a large number of active sites, improved oxidation activity, and the ability to transfer and separate charge carriers, and owing to these benefits, the PNT/CuO GCE showed high activity as an electrocatalyst for the production of H_2 and sensitivity. The fabricated PNT/CuO GCE was used for the electrochemical detection of HQ analyte and its CV curve shows a wide area under the curve with good redox activity. The DPV analysis of PNT/CuO GCE showed that it possessed a low LOD of 0.36 μM and the linear range was found to be 5 μM to 60 μM with an achieved sensitivity of 9.33 $\mu A\ \mu M^{-1}\ cm^{-2}$, and the real sample analysis of HQ detection demonstrated outstanding recovery results of 97.45% to 102.61% with an RSD of 1%. These results signify that the fabricated PNT/CuO GCE has a good performance as a sensor for practical application in the biomedical, environmental, and pharmaceutical fields. In addition, PNT/CuO GCE exhibited outstanding electrocatalyst activity for HER, with $\eta = 330$ mV and Tafel slope = 139 mV dec^{-1}. These data revealed that the PNT/CuO GCE composition demonstrated increased electrocatalyst activity towards H_2 production. Thus, this study reported the synthesis of an efficient conducting polymer-doped metal oxide electrocatalyst for electrochemical detection and HER application.

Data availability

The authors confirm that the all data supporting the findings of this study are available within the article and its ESI.†

Conflicts of interest

There are no conflicts to declare.

Acknowledgements

The authors acknowledge the PURSE Lab for the characterization facility, Mangalore University, Karnataka, India. This research received funding support from the National Science, Research and Innovation Fund (NSRF) *via* the Program Management Unit for Human Resources & Institutional Development and Innovation (PMU-B) sanctioned grant no. B13F670067, Bangkok, Thailand.

References

1 H. Zhang, X. Yang, H. Wang, Y. Wang, R. Li, H. Fu and T. Yang, Vanadium modulated Ni-$MoSe_2$ as highly efficient electrocatalyst for alkaline hydrogen evolution, *J. Mol. Struct.*, 2024, 141132.

2 A. Mohan and S. Sharma, In-situ carbon integration on atomically dispersed platinum metal oxide nanocomposites for hydrogen evolution reaction, *Electrochim. Acta*, 2024, **508**, 145218.

3 A. Guboova, R. Orinakova, M. Streckova, N. Podrojkova, M. Paracková, O. Milkovic and T. Bystron, Bimetallic MoFe phosphide catalysts for the hydrogen evolution reaction, *Electrochim. Acta*, 2024, **506**, 145008.

4 Z. Qiu, X. Guo, S. Cao, M. Du, Q. Wang, Y. Pi and H. Pang, High-Entropy Ag–Ru-Based Electrocatalysts with Dual-Active-Center for Highly Stable Ultra-Low-Temperature Zinc-Air Batteries, *Angew. Chem., Int. Ed.*, 2025, **64**(3), e202415216.

5 I. B. Isik, D. Kaya, H. H. Isik, A. Ekicibil and F. Karadag, Bifunctional bimetallic PtNi, PtCu, and NiCu nanoparticles: Electrocatalytic activities for hydrogen evolution reaction and magnetic properties, *Mater. Sci. Eng., B*, 2024, **300**, 117081.

6 M. Du, B. Chu, Q. Wang, C. Li, Y. Lu, Z. Zhang and Q. Xu, Dual Fe/I Single-Atom Electrocatalyst for High-Performance Oxygen Reduction and Wide-Temperature Quasi-Solid-State Zn-Air Batteries, *Adv. Mater.*, 2024, **36**(47), 2412978.

7 S. Cogal, G. C. Cogal, M. Micusik, A. Michalcova, M. Slouf and M. Omastova, Conducting polymer-templated and nonnoble metal doped $MoSe_2$ hybrids as bifunctional electrocatalysts for overall water splitting, *J. Electroanal. Chem.*, 2023, **946**, 117728.

8 Y. Dang, X. Wang, R. Cui, S. Chen and Y. Zhou, A novel electrochemical sensor for the selective determination of hydroquinone and catechol using synergic effect of electropolymerized nicotinic acid film and Cd-doped $ZnWO_4$ nanoneedle, *J. Electroanal. Chem.*, 2019, **834**, 196–205.

9 R. Huang, D. Liao, S. Chen, J. Yu and X. Jiang, A strategy for effective electrochemical detection of hydroquinone and catechol: Decoration of alkalization-intercalated Ti_3C_2 with MOF-derived N-doped porous carbon, *Sens. Actuators, B*, 2020, **320**, 128386.

10 B. K. Swamy and J. K. Shashikumara, Poly(benzydamine) sensor for electrochemical resolution of catechol and hydroquinone, *Mater. Sci. Energy Technol.*, 2020, **3**, 640–647.

11 B. Zhu, D. T. Bryant, A. Akbarinejad, J. Travas-Sejdic and L. I. Pilkington, A novel electrochemical conducting polymer sensor for the rapid, selective and sensitive detection of biothiols, *Polym. Chem.*, 2022, **13**(4), 508–516.

12 E. N. Heybet, V. Ugraskan, B. Isik and O. Yazici, Adsorption of methylene blue dye on sodium alginate/polypyrrole nanotube composites, *Int. J. Biol. Macromol.*, 2021, **193**, 88–99.

13 A. A. M. Elnaggar, L. A. Alsulaymani, A. A. Alsaleh, A. M. Kamal and A. A. Albassam, Exploring the optical and electrical features of PVA/CMC/PPy/MWCNTs blended polymers, *Opt. Mater.*, 2024, **155**, 115878.

14 S. Li, T. Wang, Z. Yang, J. He, J. Wang, L. Zhao and G. Lu, Room temperature high performance NH_3 sensor based on GO-rambutan-like polyaniline hollow nanosphere hybrid assembled to flexible PET substrate, *Sens. Actuators, B*, 2018, **273**, 726–734.

15 S. Alamri, A. A. Rajhi, A. E. Anqi and N. Tran, Enhanced microwave dissipation features of $BiFe_{0.8}Co_{0.1}Mn_{0.1}O_3$/MWCNTs composite decorate of polythiophene, *J. Magn. Magn. Mater.*, 2022, **545**, 168724.

16 G. Liu, M. Ma, H. Meng, J. Liu, Y. Zheng, J. Peng and J. Li, In-situ self-assembly of bacterial cellulose/poly(3,4-ethylenedioxythiophene)-sulfonated nanofibers for peripheral nerve repair, *Carbohydr. Polym.*, 2022, **281**, 119044.

17 L. Li, G. Li and B. An, Synthesis of a DWNTs/PAni composite and its supercapacitive behavior compared to the SWNTs/PAni and MWNTs/PAni composites, *RSC Adv.*, 2014, **4**(19), 9756–9761.

18 S. P. Vijaykumar, S. Sapna, D. S. Suresh, H. Ganesha, S. Veeresh, Y. S. Nagaraju and H. Devendrappa, Micelles self-degraded template based 2D graphitic carbon nitride-polypyrrole nanotube composite electrode for high supercapacitor performance, *Diamond Relat. Mater.*, 2023, **139**, 110257.

19 R. Liu, J. Duay, T. Lane and S. B. Lee, Synthesis and characterization of RuO_2/poly(3,4-ethylenedioxythiophene) composite nanotubes for supercapacitors, *Phys. Chem. Chem. Phys.*, 2010, **12**(17), 4309–4316.

20 C. A. Zito, T. M. Perfecto, C. S. Fonseca and D. P. Volanti, Effective reduced graphene oxide sheets/hierarchical flower-like NiO composites for methanol sensing under high humidity, *New J. Chem.*, 2018, **42**(11), 8638–8645.

21 N. Wang, S. Peng, X. Chen, J. Wang, C. Wang, X. Qi and S. Yan, Construction of ultrathin MnO_2 decorated graphene/carbon nanotube nanocomposites as efficient sulfur hosts for high-performance lithium–sulfur batteries, *RSC Adv.*, 2019, **9**(11), 6346–6355.

22 J. W. Lee, S. Y. Lim, H. M. Jeong, T. H. Hwang, J. K. Kang and J. W. Choi, Extremely stable cycling of ultra-thin V_2O_5 nanowire–graphene electrodes for lithium rechargeable battery cathodes, *Energy Environ. Sci.*, 2012, **5**(12), 9889–9894.

23 R. Ramasamy, K. Ramachandran, G. G. Philip, R. Ramachandran and H. A. Therese, Design and development of Co_3O_4/NiO composite nanofibers for the application of highly sensitive and selective non-enzymatic glucose sensors, *RSC Adv.*, 2015, **5**(93), 76538–76547.

24 J. M. Yang, W. Zhang, Q. Liu and W. Y. Sun, Porous ZnO and ZnO–NiO composite nano/microspheres: synthesis, catalytic and biosensor properties, *RSC Adv.*, 2014, **4**(93), 51098–51104.

25 K. Yang, Y. Yan, H. Wang, Z. Sun, W. Chen, H. Kang and Z. Li, Monodisperse $Cu/Cu_2O@C$ core–shell nanocomposite supported on rGO layers as an efficient catalyst derived from a Cu-based MOF/GO structure, *Nanoscale*, 2018, **10**(37), 17647–17655.

26 H. Mahajan and S. Cho, Novel Au nanorod/Cu_2O composite nanoparticles for a high-performance supercapacitor, *RSC Adv.*, 2022, **12**(15), 9112–9120.

27 A. Martínez-García, V. K. Vendra, S. Sunkara, P. Haldankar, J. Jasinski and M. K. Sunkara, Tungsten oxide-coated copper oxide nanowire arrays for enhanced activity and durability with photoelectrochemical water splitting, *J. Mater. Chem. A*, 2013, **1**(48), 15235–15241.

28 J. Zhao, X. Shu, Y. Wang, C. Yu, J. Zhang, J. Cui and Y. Wu, Construction of $CuO/Cu_2O@CoO$ core shell nanowire arrays for high-performance supercapacitors, *Surf. Coat. Technol.*, 2016, **299**, 15–21.

29 P. Basu, R. Mahesh, S. Harish, S. Joseph and P. Sagayaraj, One-pot hydrothermal preparation of Cu_2O-CuO/rGO nanocomposites with enhanced electrochemical performance for supercapacitor applications, *Appl. Surf. Sci.*, 2018, **449**, 474–484.

30 W. Zhang, X. He, Q. Li, L. Feng, X. Cao and D. Chen, Three-dimensional "skin-core" structures of FeCe co-doped PPy@FCC-ZIF by in-situ ion exchange etching to used stabilize water electrolysis in high current density, *J. Electroanal. Chem.*, 2024, 118891.

31 M. J. Saadh, D. J. Jasim, L. Alejandro, S. K. Saraswat, C. G. F. Arevalo, N. A. E. Brito and S. Islam, Harnessing the potential of MOF/Fe_2O_3 nanocomposite within polypyrrole matrix for enhanced hydrogen evolution, *Electrochim. Acta*, 2024, **507**, 145157.

32 R. Tan, M. J. Kang, L. Qu, S. W. Hwang, S. Y. Hong, Y. J. Jeong and I. S. Cho, Solution-processed nanoporous and faceted CuO electrocatalyst for enhanced solar-to-hydrogen and nitrate-to-ammonia production, *J. Water Proc. Eng.*, 2024, **61**, 105322.

33 U. Younas, F. Mobeen, A. Saleem, F. Ali, M. Al Huwayz, A. Ashraf and M. Iqbal, Efficient hydrogen production via overall water splitting using CuO/ZnO decorated reduced graphene oxide as bifunctional electrocatalyst, *Ceram. Int.*, 2024, **50**(17), 30570–30578.

34 M. P. Kumar, N. Kumaresan, R. V. Mangalaraja, I. Zaporotskova, A. Arulraj, G. Murugadoss and A. Pugazhendhi, Zinc oxide nanoflakes supported copper oxide nanosheets as a bifunctional electrocatalyst for OER and HER in an alkaline medium, *Environ. Res.*, 2024, **252**, 119030.

35 H. Veisi, B. Karmakar, T. Tamoradi, S. Hemmati, M. Hekmati and M. Hamelian, Biosynthesis of CuO nanoparticles using aqueous extract of herbal tea (Stachys Lavandulifolia) flowers and evaluation of its catalytic activity, *Sci. Rep.*, 2021, **11**(1), 1–13.

36 M. Majumder, R. B. Choudhary, A. K. Thakur and I. Karbhal, Impact of rare-earth metal oxide (Eu_2O_3) on the electrochemical properties of a polypyrrole/CuO polymeric composite for supercapacitor applications, *RSC Adv.*, 2017, **7**(32), 20037–20048.

37 N. He, X. Yang, L. Shi, X. Yang, Y. Lu, G. Tong and W. Wu, Chemical conversion of Cu_2O/PPy core-shell nanowires (CSNWs): A surface/interface adjustment method for high-quality Cu/Fe/C and Cu/Fe_3O_4/CCSNWs with superior microwave absorption capabilities, *Carbon*, 2020, **166**, 205–217.

38 H. U. Khan, M. Tariq, M. Shah, M. Iqbal and M. T. Jan, Inquest of highly sensitive, selective and stable ammonia (NH_3) gas sensor: structural, morphological and gas sensing properties of polyvinylpyrrolidone (PVP)/CuO nanocomposite, *Synth. Met.*, 2020, **268**, 116482.

39 N. Baylan, I. Ilalan and I. Inci, Copper oxide nanoparticles as a novel adsorbent for separation of acrylic acid from

aqueous solution: synthesis, characterization, and application, *Water, Air, Soil Pollut.*, 2020, **231**(9), 1–15.

40 S. Selvarajan, A. Suganthi and M. Rajarajan, A novel highly selective and sensitive detection of serotonin based on Ag/polypyrrole/Cu_2O nanocomposite modified glassy carbon electrode, *Ultrason. Sonochem.*, 2018, **44**, 319–330.

41 M. Vandana, S. Veeresh, H. Ganesh, Y. S. Nagaraju, H. Vijeth, M. Basappa and H. Devendrappa, Graphene oxide decorated SnO_2 quantum dots/polypyrrole ternary composites towards symmetric supercapacitor application, *J. Energy Storage*, 2022, **46**, 103904.

42 M. Abdelfatah, A. Basuni, H. Y. Salah, M. Bakry, N. Darwesh, W. Ismail and A. El Shaer, Improvement of physical and electrochemical properties of Cu_2O thin films with Fe ions doping towards optoelectronic applications, *Opt. Mater.*, 2022, **130**, 112583.

43 S. Y. Zhen, H. T. Wu, Y. Wang, N. Li, H. S. Chen, W. L. Song and K. N. Sun, Metal–organic framework derived hollow porous CuO–$CuCo_2O_4$ dodecahedrons as a cathode catalyst for Li–O_2 batteries, *RSC Adv.*, 2019, **9**(29), 16288–16295.

44 Z. Jin, C. Liu, K. Qi and X. Cui, Photo-reduced Cu/CuO nanoclusters on TiO_2 nanotube arrays as highly efficient and reusable catalyst, *Sci. Rep.*, 2017, **7**(1), 1–9.

45 J. Jiang, X. X. Liu, J. Han, K. Hu and J. S. Chen, Self-Supported Sheets-on-Wire CuO@Ni$(OH)_2$/Zn$(OH)_2$ Nanoarrays for High-Performance Flexible Quasi-Solid-State Supercapacitor, *Processes*, 2021, **9**(4), 680.

46 H. Siddiqui, M. S. Qureshi and F. Z. Haque, Biosynthesis of flower-shaped CuO nanostructures and their photocatalytic and antibacterial activities, *Nano-Micro Lett.*, 2020, **12**(1), 1–11.

47 N. He, X. Yang, L. Shi, X. Yang, Y. Lu, G. Tong and W. Wu, Chemical conversion of Cu_2O/PPy core-shell nanowires (CSNWs): A surface/interface adjustment method for high-quality Cu/Fe/C and Cu/Fe_3O_4/CCSNWs with superior microwave absorption capabilities, *Carbon*, 2020, **166**, 205–217.

48 B. Lu, J. Liu, R. Hu, H. Wang, J. Liu and M. Zhu, C@MoS_2@PPy sandwich-like nanotube arrays as an ultrastable and high-rate flexible anode for Li/Na-ion batteries, *Energy Storage Mater.*, 2018, **14**, 118–128.

49 Y. Liu, S. Liu, J. Jiang, X. Wei, K. Zhao, R. Shen and B. Li, Monomolecule Coupled to Oxygen-Doped Carbon for Efficient Electrocatalytic Hydrogen Peroxide Production, *Adv. Mater.*, 2025, **37**(14), 2502197.

50 X. Yang, Y. Tian, S. Sarwar, M. Zhang, H. Zhang, J. Luo and X. Zhang, Comparative evaluation of PPyNF/CoOx and PPyNT/CoOx nanocomposites as battery-type supercapacitor materials via a facile and low-cost microwave synthesis approach, *Electrochim. Acta*, 2019, **311**, 230–243.

51 M. Dhanda, R. Arora, A. S. Reddy, S. Lata and A. Sharma, Coalescing of lanthanum oxide and PPy@graphitic carbon nitride to achieve ultrahigh energy density electrode material for supercapacitors applications, *J. Alloys Compd.*, 2023, **955**, 169738.

52 R. Zainul, C. Y. Hsu, A. Basem, D. J. Jasim, A. A. S. Conde, Y. Ajaj and A. Elawady, In-situ growth of MCo_2O_4 nanospheres (M: Mn, Ni) over g-C_3N_4@PPy as high-performance and novel composites for sustainable supercapacitors, *J. Energy Storage*, 2024, **90**, 111727.

53 A. Pasha, S. Khasim, A. A. A. Darwish, T. A. Hamdalla and S. A. Al-Ghamdi, High performance organic coatings of polypyrrole embedded with manganese iron oxide nanoparticles for corrosion protection of conductive copper surface, *J. Inorg. Organomet. Polym. Mater.*, 2022, 1–14.

54 K. Yamani, R. Berenguer, A. Benyoucef and E. Morallon, Preparation of polypyrrole (PPy)-derived polymer/ZrO_2 nanocomposites: Effects of nanoparticles interface and polymer structure, *J. Therm. Anal. Calorim.*, 2019, **135**, 2089–2100.

55 P. M. Nia, W. P. Meng, F. Lorestani, M. R. Mahmoudian and Y. Alias, Electrodeposition of copper oxide/polypyrrole/reduced graphene oxide as a nonenzymatic glucose biosensor, *Sens. Actuators, B*, 2015, **209**, 100–108.

56 S. M. Oliveira, J. M. Luzardo, L. A. Silva, D. C. Aguiar, C. A. Senna, R. Verdan and J. R. Araujo, High-performance electrochemical sensor based on molecularly imprinted polypyrrole-graphene modified glassy carbon electrode, *Thin Solid Films*, 2020, **699**, 137875.

57 Y. Xia, K. Wang, Y. Shi, X. Gui, C. Lv and H. Tao, Reduced graphene oxide cross-linked L-cysteine modified glassy carbon electrode for detection of environmental pollutant of hydroquinone, *FlatChem*, 2021, **25**, 100214.

58 H. Huang, Y. Chen, Z. Chen, J. Chen, Y. Hu and J. J. Zhu, Electrochemical sensor based on Ce-MOF/carbon nanotube composite for the simultaneous discrimination of hydroquinone and catechol, *J. Hazard. Mater.*, 2021, **416**, 125895.

59 C. M. Kuskur, B. K. Swamy and H. Jayadevappa, Poly (Evans blue) sensor for catechol and hydroquinone: a voltammetric study, *J. Electroanal. Chem.*, 2019, **833**, 512–519.

60 T. Lai, W. Cai, W. Dai and J. Ye, Easy processing laser reduced graphene: a green and fast sensing platform for hydroquinone and catechol simultaneous determination, *Electrochim. Acta*, 2014, **138**, 48–55.

61 S. J. Li, C. Qian, K. Wang, B. Y. Hua, F. B. Wang, Z. H. Sheng and X. H. Xia, Application of thermally reduced graphene oxide modified electrode in simultaneous determination of dihydroxybenzene isomers, *Sens. Actuators, B*, 2012, **174**, 441–448.

62 J. Da Silva Hortencio, A. De Almeida Lourenco, R. A. Raimundo, R. B. Da Silva, D. A. Macedo, S. G. Lemos and F. F. Da Silva, MOF-templated CuO and MnCuO/Cu_2O composites as electrocatalyst in oxygen evolution, *J. Mol. Struct.*, 2024, **1297**, 137018.

63 H. Wu, T. Wan, W. Gao, Y. Lv, J. Zhang and Q. Shen, Two mononuclear ferrous complexes as molecular electrocatalysts immobilized on carbon paste electrodes for the hydrogen evolution reaction, *J. Mol. Struct.*, 2023, **1294**, 136408.

64 Y. Lv, W. Gao, J. Zhang, C. Fei, Z. Wu and H. Wu, Electrodes composited by bisbenzimidazole silver(I) coordination polymers as electrocatalysts for hydrogen evolution and H_2O_2-sensing, *Inorg. Chim. Acta*, 2024, 122164.

65 S. Pavithra, Conducting polymer encrusted Cu/Mn-MOF-CNDs: A facile synthesis, characterization and its hydrogen evolution activity in alkaline media and seawater, *Synth. Met.*, 2023, **297**, 117422.

66 X. F. Li, M. Y. Lu, H. Y. Yu, T. H. Zhang, J. Liu, J. H. Tian and R. Yang, Copper-Metal Organic Frameworks Electrodeposited on Carbon Paper as an Enhanced Cathode for the Hydrogen Evolution Reaction, *ChemElectroChem*, 2019, **6**(17), 4507–4510.